JOURNAL OF MICROELECTROMECHANICAL SYSTEMS, VOL. 17, NO. 1, FEBRUARY 2008

Single- and Triaxis Piezoelectric-Bimorph Accelerometers

Qiang Zou, *Member, IEEE*, Wei Tan, Eun Sok Kim, *Senior Member, IEEE*, and Gerald E. Loeb, *Member, IEEE*

***Abstract*—This paper describes the novel single- and triaxis piezoelectric-bimorph accelerometers that are built on parylene beams with ZnO films. The unamplified sensitivity and the minimum detectable signal of the fabricated single-axis accelerometer are measured to be 7.0 mV/g and 0.01 g, respectively, over a frequency range from 60 Hz to subhertz. The linearity of the sensitivity as a function of acceleration is measured to be 0.9% in the full scale. A highly symmetric quad-beam bimorph structure with a single proof mass is used for triaxis acceleration sensing and is demonstrated to produce high sensitivity, low cross-axial sensitivity, and good linearity, all in a compact size. The unamplified sensitivities of the X-, Y-, and Z-axis electrodes (of the triaxis accelerometer) in response to the accelerations in X-, Y-, and Z-axes are 0.93, 1.13, and 0.88 mV/g, respectively. The worst-case minimum detectable signal of the triaxis accelerometer is measured to be 0.04 g over a bandwidth ranging from subhertz to 100 Hz. The cross-axial sensitivity among the X-, Y-, and Z-axis electrodes is less than 15% in the triaxis accelerometer. The theoretical analyses of the charge sensitivities and resonant frequencies along with the effects of residual stress on the charge sensitivities are presented for both the single- and triaxis accelerometers. [1686]**

***Index Terms*—Parylene beam, piezoelectric accelerometer, piezoelectric bimorph, triaxis piezoelectric accelerometer.**

I. INTRODUCTION

MICROMACHINED accelerometers are highly desirable for inertial navigation, stability, and rollover control of automobile and for biomedical instrumentation because of their small size, particularly if combined with low cost, high performance, and low power consumption. Various micromachined accelerometers have already been developed based on capacitive, piezoresistive, resonant, tunneling, thermal, and piezoelectric sensing methods [1]–[6]. Among the micromachined silicon accelerometers, the piezoresistive and capacitive approaches have been most popular due to easiness of fabrication and high sensitivity, respectively. However, piezoresistive sensing consumes inherently high power, whereas capacitive sensing requires rather elaborate electronics that is often power hungry. Moreover, piezoresistors tend to drift in time due to heating by the bias current. In addition, capacitive sensors require narrow air gap over a relatively large area, which overdamps, and sometimes squeeze-film damps, and limits the usable frequency bandwidth.

A piezoelectric accelerometer, on the other hand, has the advantages of extremely low power consumption, simple detection circuit, high sensitivity, and inherent temperature stability. Thus, we have developed piezoelectric accelerometers to be integrated into an implantable neuromuscular stimulator called the BION [7] that is cylindrical with 20-mm length and 2-mm diameter (shown in Fig. 1). The accelerometers are used to sense human body movement and provide BION with the acceleration of the body or its inclination with respect to the gravitational field. Consequently, the accelerometers have to be very compact, extremely low power consuming, highly sensitive, and insensitive to cross-axis accelerations. The specifications of the MEMS accelerometer for BION application are shown in Table I.

The micromachined piezoelectric accelerometers have typically relied on bulk micromachining [8]–[11] and surface micromachining techniques [12], [13] to produce a spring-mass structure. Some finite-element-method simulations on triaxis piezoelectric-unimorph accelerometers that are built on very thin silicon beams have been reported [14], [15]. However, very few theoretical analyses and experimental results on triaxis piezoelectric accelerometers have been reported.

All of the previously reported micromachined piezoelectric accelerometers use single crystal silicon, polysilicon, or $\mathrm{Si}_x\mathrm{N}_y$ as a supporting beam. Nevertheless, the high stiffness and residual stress of these materials limit the accelerometers' performance. Usage of parylene as a support diaphragm for piezoelectric acoustic transducers was reported in [16]–[18] and had shown to improve the sensitivities due to parylene's very low Young's modulus (~3.2 GPa) and nonbrittle characteristics. When parylene film is used as a support beam for piezoelectric accelerometers, it is difficult to place the neutral plane outside the piezoelectric layer with a unimorph structure because of the extremely low stiffness of parylene. Thus, we use a bimorph structure with two ZnO piezoelectric films of opposite C-axis orientations to make the neutral plane location outside of the ZnO films and to maximize the sensitivities of the accelerometers. In this paper, the mechanical structure design, theoretical analysis, fabrication, and measurement results of the single- and triaxis piezoelectric-bimorph accelerometers are presented.

Manuscript received September 7, 2005; revised April 22, 2006. Subject Editor M. Mehregany.

Q. Zou was with the Department of Electrical Engineering, University of Southern California, Los Angeles, CA 90089 USA. He is currently with the Wireless Semiconductor Division, Avago Technologies, Ltd., San Jose, CA 95131 USA (e-mail: qiang.zou@avagotech.com).

W. Tan and G. E. Loeb are with the Alfred E. Mann Institute for Biomedical Engineering, University of Southern California, Los Angeles, CA 90089 USA.

E. S. Kim is with the Department of Electrical Engineering, University of Southern California, Los Angeles, CA 90089 USA.

Color versions of one or more of the figures in this paper are available online at http://ieeexplore.ieee.org.

Digital Object Identifier 10.1109/JMEMS.2007.909100

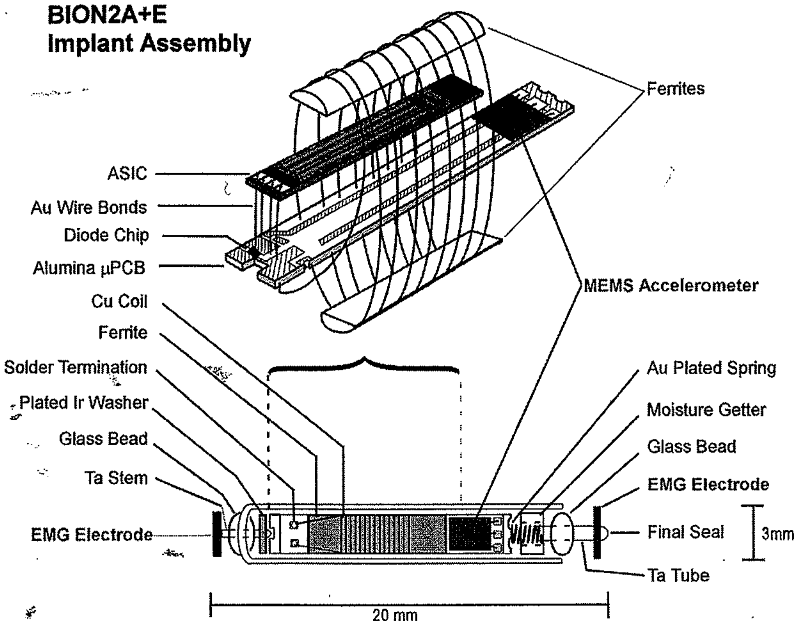

Fig. 1. Schematic view of BION with MEMS accelerometer.

TABLE I
ACCELEROMETER SPECIFICATIONS FOR BION APPLICATION

Chip size	**< 3×1.2×0.6 mm^3**
Power consumption	**< 0.5mW**
Bandwidth	**DC to 20Hz**
Dynamic range	**-1g~1g**
Resolution	**0.01g**

II. SENSOR STRUCTURES

A. Single-Axis Piezoelectric-Bimorph Accelerometer

The single-axis piezoelectric-bimorph accelerometer with a beam-mass structure is schematically shown in Fig. 2. The beam consists of parylene/Al/Si_xN_y/ZnO/Si_xN_y/Al/Si_xN_y/ZnO/Si_xN_y/Al/parylene multiple layers. The neutral plane is just at the middle of the symmetric bimorph beam. Parylene is used because of the following reasons: 1) It has a very small Young's modulus ($\sim$3.2 GPa) and adds negligible stiffness to the sensing structure, and 2) it is a nonbrittle plastic material with a very large linear elastic range (its yield strain being $\sim$3%). Moreover, parylene is moisture-blocking, chemically inert, electrically insulating, and biocompatible.

In order to make the neutral plane location outside of the piezoelectric films, a bimorph structure with two oppositely oriented 0.3-μm ZnO piezoelectric films is used. Each of the ZnO films is encapsulated with two 0.1-μm-thick plasma-enhanced chemical-vapor-deposited (PECVD) Si_xN_y insulating layer to improve the accelerometer's low-frequency response so that the accelerometer has a quasi-dc response [19]. A 0.4-μm-thick Al is used for the top, middle, and bottom electrodes. The middle Al electrode (buried between two piezoelectric films) is electrically floating. The piezoelectric-bimorph beam is mechanically supported by two thick parylene layers (1.0–5.0 μm thick) on the top and bottom of the bimorph.

When Z-axis acceleration is applied to the structure, the proof mass is displaced such that the bimorph beam goes through bending, producing tensile and compressive stresses above and below the neutral plane. Because of the opposite C-axis orientations of the ZnO films on the top and bottom of the neutral plane, the opposite distribution of the stress above and below the neutral plane will produce a voltage (between the top and bottom electrodes) that is the sum of the voltages developed between the top and middle electrodes and between the middle and bottom electrodes. The thickness and material properties of the layers used in the piezoelectric bimorph are summarized in Table II.

B. Triaxis Piezoelectric-Bimorph Accelerometer

Fig. 3 shows the schematic of the triaxis accelerometer with a single seismic mass suspended by four symmetric parylene/Al/Si_xN_y/ZnO/Si_xN_y/Al/Si_xN_y/ZnO/Si_xN_y/Al bimorph beams. The electrodes on the top side of the four beams are segmented into Z_1, Z_2, Z_3, Z_4 (for Z-axis sensing), X_1, X_2 (for X-axis sensing), and Y_1 and Y_2 (for Y-axis sensing) (Fig. 3). The operating principle of the triaxis accelerometer is shown in Fig. 4. When the seismic mass is accelerated vertically (along the Z-axis), it produces tensile stress in the top half of the bimorph in X_1, X_2, Y_1, and Y_2 and compressive stress in Z_1–Z_4. Furthermore, there exists a finite voltage (V_z) between the parallel-connected Z_1–Z_4 and the electrode on the other face of the diaphragm because the top and bottom halves of the bimorph have opposite stress distribution. However, the voltage (V_x) between X_1 and X_2 (and also V_y between Y_1 and Y_2) is almost zero because the net stress between the two electrodes is zero. When the seismic mass is accelerated laterally (e.g., in X-direction), it rotates around Y-axis and produces tensile stress in X_1 and Z_3 and compressive stress in Z_1 and X_2. It also produces shear stress in Y_1, Y_2, Z_2, and Z_4, which can be neglected. Thus, acceleration along X-direction

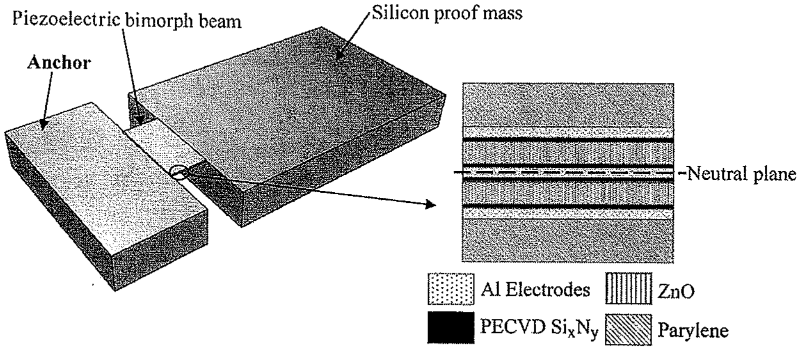

Fig. 2. Schematic view of the single-axis piezoelectric-bimorph accelerometer.

TABLE II
THICKNESS AND MATERIAL PROPERTIES OF THE LAYERS USED IN THE SINGLE-AXIS PIEZOELECTRIC-BIMORPH ACCELEROMETER

Material	Thickness (μm)	Materials properties (Young's modulus, Poisson's ratio, Density)
Al	0.4	E=69GPa, 0.33, 2700kg/m^3
Parylene	1.0 ~ 5.0	E=3.2GPa, 0.4, 1289kg/m^3
ZnO	0.3	C_{11}=210GPa, C_{12}=120GPa, C_{13}=105GPa, C_{33}=210GPa, C_{44}=43GPa, 5700kg/m^3
Si_xN_y	0.1	E=272GPa, 0.25, 3100kg/m^3

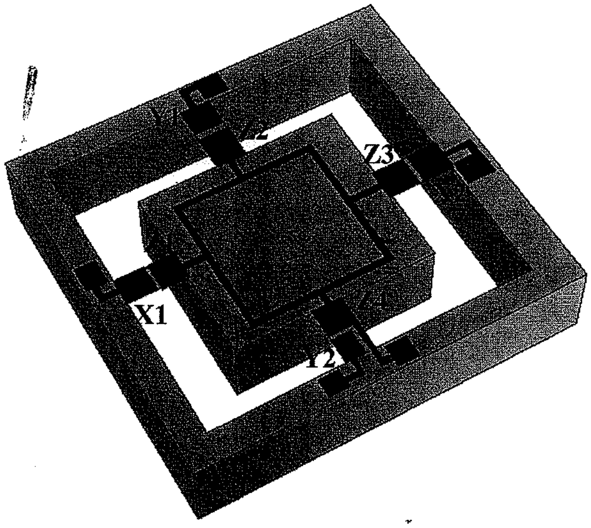

Fig. 3. Schematic view of the triaxis piezoelectric-bimorph accelerometer.

produces a finite differential signal V_x but almost zero V_y and V_z because of zero net stress between Y_1 and Y_2 and of Z_1 and Z_3 canceling each other, respectively. The same principles apply to the case in which the seismic mass is accelerated laterally in Y-direction.

III. THEORETICAL ANALYSIS ON MECHANICAL DESIGN

In order to predict the sensor performance and optimize the mechanical design, we formulate and analyze the charge sensitivity and mechanical resonant frequency for the single- and triaxis piezoelectric-bimorph accelerometers. For a piezoelectric ZnO film on a cantilever beam with the cantilever's length in X-direction, the electrical-field displacement D in Z-direction (i.e., the thickness direction) is related to the Z-directed electrical field (E_{field}) and X-directed normal stress (σ), which is generated by the cantilever bending as follows:

$$D = \varepsilon E_{\text{field}} + d_{31}\sigma \tag{1}$$

where ε and $d_{31}(= 2.3 \times 10^{-12}$ C/N for ZnO [13]) are the permittivity and piezoelectric coefficient of the piezoelectric film, respectively.

For piezoelectric sensing, we usually do not apply any external electric field, and (1) can be simplified to

$$D = d_{31}\sigma. \tag{2}$$

The normal stress in X-direction (produced in a piezoelectric film of a bimorph cantilever by a pure bending) can be obtained by the following [20]:

$$\sigma = E_{\text{p}} \cdot \frac{1}{R} \cdot z_{\text{p}} = E_{\text{p}} \cdot \frac{M}{\sum_i E_i\left(I_i + A_i Z_i^2\right)} \cdot z_{\text{p}} \tag{3}$$

where E_{p} is the Young's modulus of the piezoelectric film, $1/R$ is the bending curvature of the bimorph cantilever beam by pure bending moment M, z_{p} is the distance between the center of the piezoelectric film and bending neutral plane, E_i is the Young's modulus of each layer in the bimorph beam, I_i is the area moment of inertia for each layer in the bimorph beam, A_i is the cross-section area of each layer in the bimorph beam, and Z_i is the distance between the center of each layer and neutral plane of the bimorph beam. Thus, the charge produced on the electrode is

$$\begin{aligned} Q &= \int D \cdot w \cdot dl \\ &= \int d_{31} \cdot E_p \cdot \frac{M}{\sum_i E_i\left(I_i + A_i Z_i^2\right)} \cdot z_p \cdot w \cdot dl \end{aligned} \tag{4}$$

where w and dl are the sensing electrode width and elemental length, respectively.

A. Single-Axis Piezoelectric-Bimorph Accelerometer

When the sensor is subject to acceleration (of magnitude acc) in Z-direction, the inertial force of the proof mass induces a deflection of the bimorph beam suspension according to the

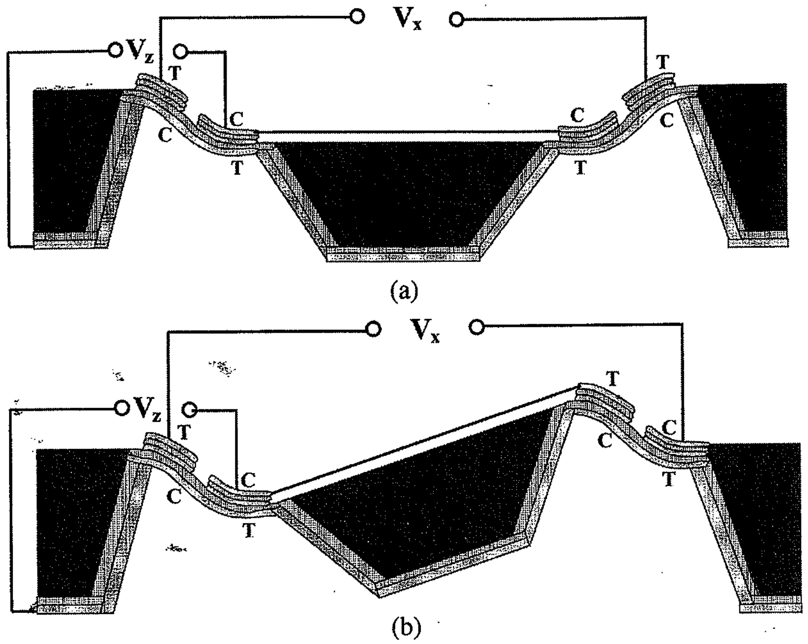

Fig. 4. Operating principle of the triaxis piezoelectric-bimorph accelerometer: (a) When vertical acceleration is applied (Z-axis) and (b) when lateral acceleration is applied (X- or Y-axis).

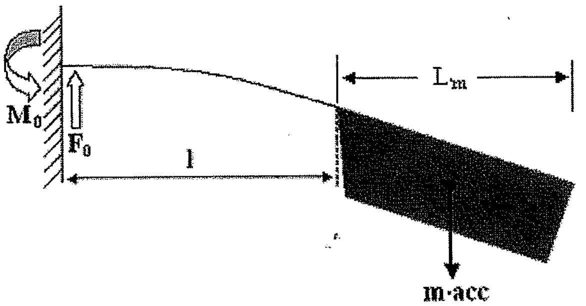

Fig. 5. Free-body diagram of the single-axis piezoelectric-bimorph accelerometer when Z-axis acceleration is applied.

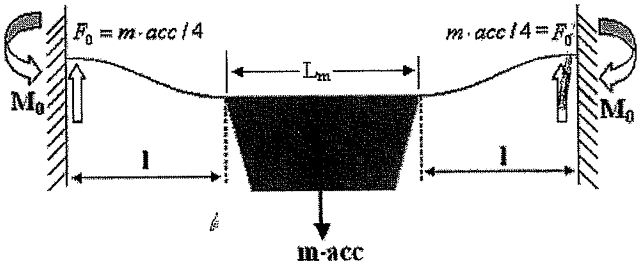

Fig. 6. Free-body diagram of the triaxis piezoelectric-bimorph accelerometer when Z-axis acceleration is applied.

free-body diagram of the suspension beam shown in Fig. 5. Substituting the bending moment in the beam (of length l, at location x) into (4) and integrating along the suspension beam, we obtain the following equation for the charge sensitivity S_q (i.e., the charge per unit acceleration) of the single-axis piezoelectric-bimorph accelerometer

$$S_q = \frac{d_{31} \cdot E_{\mathrm{p}} \cdot z_{\mathrm{p}} \cdot m \cdot \frac{1}{2} \cdot (L_{\mathrm{m}} + l) \cdot l}{\sum_i E_i \left(\frac{1}{12} \cdot h_i^3 + h_i \cdot Z_i^2\right)} \tag{5}$$

where h_i and l are the thickness of the ith layer in the bimorph beam and the length of the suspension beam, respectively, whereas m and L_{m} are the mass and the length of the silicon proof mass, respectively. In obtaining (5), we use $I_i = w \cdot h_i^3/12$ and $A_i = w \cdot h_i$, and we see that the beam width has no effect on the charge sensitivity, as expected, since the stress equation is for a beam bending.

B. Triaxis Piezoelectric-Bimorph Accelerometer

As the triaxis accelerometer has the symmetric quad-beam structure, the X- and Y-axis sensors have the same response when X- and Y-axis accelerations are applied. In this section, we analyze the Z- and X-/Y-axis responses of the accelerometer.

1) Z-Axis Sensitivity Analysis: Fig. 6 shows a free-body diagram of the triaxis accelerometer when Z-axis acceleration is applied. The proof mass in the middle moves vertically, whereas the four suspension beams deflect with the same displacement. Solving the governing differential equation according to the boundary conditions ($(y|_{x=0} = 0$, $(dy/dx)|_{x=0} = 0$, $(dy/dx)|_{x=l} = 0$), we obtain the vertical displacement y and bending moment M in the suspension beam at a location x as follows:

$$\begin{aligned} y(x) = {} & \frac{1}{\sum_i E_i \left(I_i + A_i Z_i^2\right)} \\ & \times \left(\frac{1}{24} \cdot m \cdot \mathrm{acc} \cdot x^3 - \frac{1}{16} \cdot m \cdot \mathrm{acc} \cdot l \cdot x^2\right) \end{aligned} \tag{6}$$

$$M(x) = \frac{1}{4} \cdot m \cdot \mathrm{acc} \cdot \left(x - \frac{1}{2} l\right) \tag{7}$$

where acc and l are the acceleration applied to the proof mass and the suspension-beam length, respectively. From (7), we see that the bending moment changes its sign just at the half of the

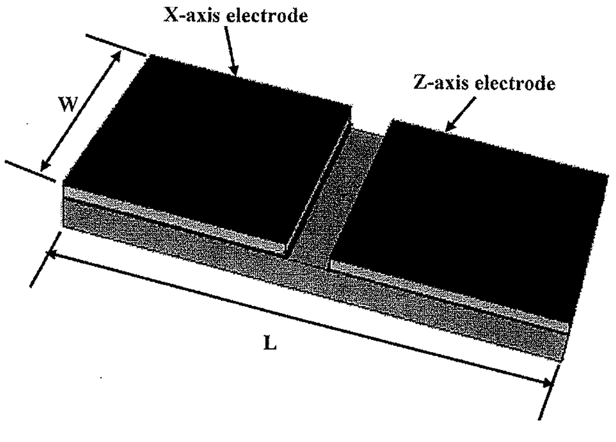

Fig. 7. Close-up view of bottom half of one suspension beam in the triaxis piezoelectric-bimorph accelerometer.

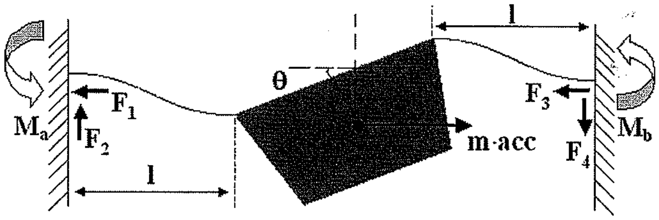

Fig. 8. Side view of the free-body diagram of the triaxis accelerometer when X-axis acceleration is applied.

beam length, which means that the stress changes its sign at the middle of the beam length, as expected.

The sensing electrodes on one suspension beam are schematically shown in Fig. 7, where the right electrode is used for Z-axis acceleration sensing, whereas the left electrode is used for X- or Y-axis acceleration sensing. Substituting (7) into (4) and integrating along the length of the Z-axis sensing electrode [from $x = (l/2)$ to $x = l$] produce the Z-axis charge sensitivity on one half of one suspension beam in the triaxis accelerometer as follows:

$$S_q = \frac{d_{31} \cdot E_{\mathrm{p}} \cdot z_{\mathrm{p}} \cdot \frac{1}{32} \cdot m \cdot l^2}{\sum_i E_i \left(\frac{1}{12} \cdot h_i^3 + h_i \cdot Z_i^2\right)}. \tag{8}$$

From (8), we again see that the charge sensitivity of the triaxis accelerometer is independent of the beam width.

2) X-/Y-Axis Sensitivity Analysis: As the X- and Y-axis sensitivities of the triaxis accelerometer are the same due to the symmetric structure, we just consider the X-axis sensitivity. The side view of the free-body diagram of the triaxis accelerometer when X-axis acceleration is applied is shown in Fig. 8. The proof mass rotates around the Y-axis beam because the center of the proof mass is not in the same plane as that of the suspension beam, resulting in a rotation angle θ (around the two Y-axis beams) and the bending moments M_{a} and M_{b} (on the two X-axis beams). In Fig. 8, the vertical displacement y needs to satisfy the following boundary conditions:

$$\begin{aligned} y|_{x=0} &= 0, \quad \left.\frac{dy}{dx}\right|_{x=0} = 0 \\ y|_{x=l} &= \frac{-L_{\mathrm{m}}}{2} \cdot \sin\theta, \quad \left.\frac{dy}{dx}\right|_{x=l} = \tan\theta. \end{aligned} \tag{9}$$

Based on the previous boundary conditions, we can obtain the vertical displacement y and bending moment M in the X-axis suspension beam at a location x as follows:

$$\begin{aligned} y(x) = {} & \frac{1}{\sum_i E_i \cdot (I_i + A_i \cdot Z_i^2)} \cdot \frac{\frac{3}{2} \cdot (l + L_{\mathrm{m}})}{k^2 \cdot l} \\ & \cdot \frac{m \cdot \mathrm{acc} \cdot \frac{H_{\mathrm{m}}}{2}}{\left[\frac{2}{1+\upsilon} + 3 \cdot \left(1 + \frac{L_{\mathrm{m}}}{l}\right)^2\right]} \\ & \cdot \left[\frac{1 - \frac{1}{2} \cdot k \cdot l}{k \cdot l} \cdot e^{k \cdot x} - \frac{1 + \frac{1}{2} \cdot k \cdot l}{k \cdot l} \cdot e^{-k \cdot x} - \frac{2}{l} \cdot x + 1\right] \end{aligned} \tag{10}$$

$$\begin{aligned} M(x) = {} & \frac{\frac{3}{2} \cdot (l + L_{\mathrm{m}})}{k \cdot l^2} \cdot \frac{m \cdot \mathrm{acc} \cdot \frac{H_{\mathrm{m}}}{2}}{\left[\frac{2}{1+\upsilon} + 3 \cdot \left(1 + \frac{L_{\mathrm{m}}}{l}\right)^2\right]} \\ & \cdot \left[\left(1 - \frac{1}{2} \cdot k \cdot l\right) \cdot e^{k \cdot x} - \left(1 + \frac{1}{2} \cdot k \cdot l\right) \cdot e^{-k \cdot x}\right] \end{aligned} \tag{11}$$

where $k = \sqrt{F_1 / \sum_i E_i \cdot (I_i + A_i \cdot Z_i^2)} = \sqrt{(1/2) \cdot m \cdot \mathrm{acc} / \sum_i E_i \cdot (I_i + A_i \cdot Z_i^2)}$, with F_1 being the lateral force applied to the suspension beam by the fixed boundary, whereas H_{m} and υ are the thickness of the silicon proof mass and the Poisson's ratio of silicon, respectively.

From (11), we see that the bending moment changes its sign at the half of the beam length, and consequently, the stress changes its sign at the half of the beam length. Substituting (11) into (4) and integrating along the length of the X-axis sensing electrode (shown in Fig. 7) produce the X-axis charge sensitivity of the triaxis accelerometer as follows:

$$S_q = \frac{d_{31} \cdot E_{\mathrm{p}} \cdot z_{\mathrm{p}}}{\sum_i E_i \left(\frac{1}{12} \cdot h_i^3 + h_i \cdot Z_i^2\right)} \cdot \frac{(l + 3 \cdot L_{\mathrm{m}}) \cdot m \cdot \frac{H_{\mathrm{m}}}{2}}{8 \cdot \left[\frac{2}{1+\upsilon} + 3 \cdot \left(1 + \frac{L_{\mathrm{m}}}{l}\right)^2\right]}. \tag{12}$$

From (12), we see that the charge sensitivity does not depend on the width of the suspension beams as long as the rotation θ is small.

C. Resonant-Frequency Analysis

Assuming the proof mass as a rigid body that keeps its dimensions without deformability [21], we obtain the following equation for the lowest resonant frequency of the single-axis accelerometer by using the Rayleigh–Ritz method:

$$\begin{aligned} f = {} & \frac{1}{2\pi} \cdot \sqrt{\frac{\sum_i E_i \left(I_i + A_i Z_i^2\right)}{\rho \cdot L_{\mathrm{m}} \cdot W_{\mathrm{m}} \cdot H_{\mathrm{m}} \cdot l^3}} \\ & \cdot \sqrt{\frac{6\alpha^2 + 12\alpha + 8}{2\alpha^4 + 7\alpha^3 + 10.5\alpha^2 + 8\alpha + \frac{8}{3}}} \end{aligned} \tag{13}$$

where $\alpha (= L_{\mathrm{m}}/l)$ is the ratio between the proof-mass and the suspension-beam lengths. Similarly, we obtain the following

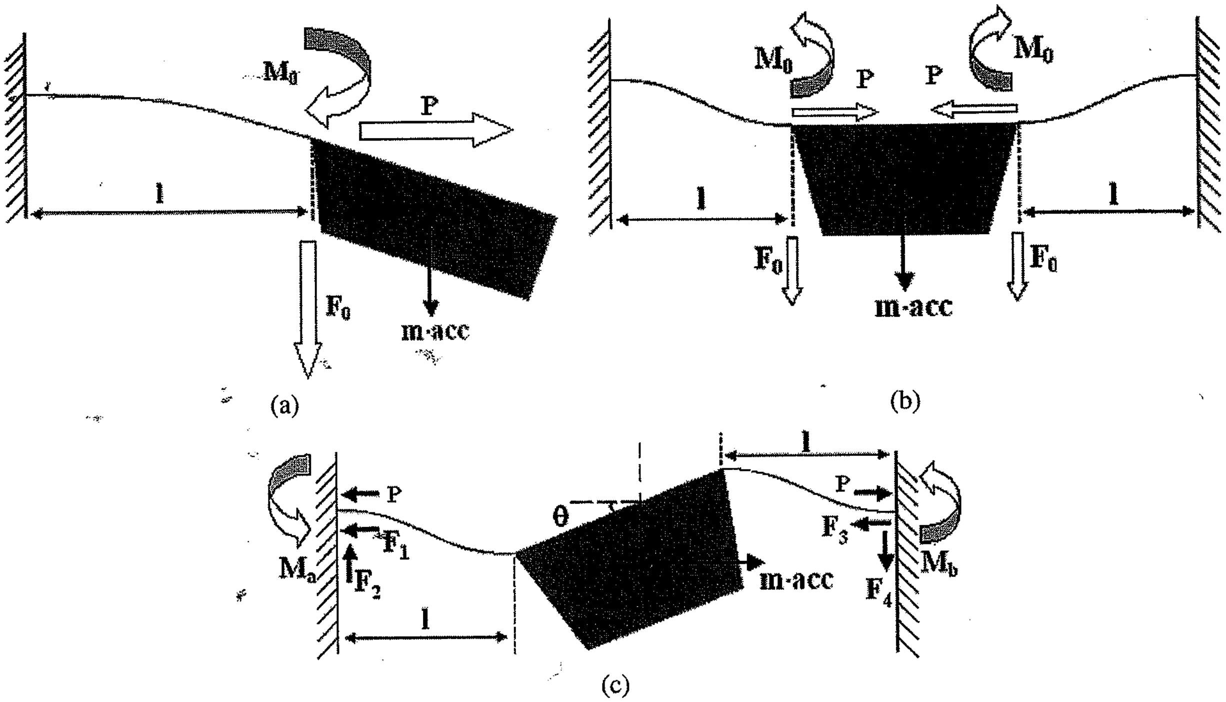

Fig. 9. Free-body diaphragms of the single- and triaxis accelerometers under in-plane residual stress in the suspending beam(s). (a) The single-axis accelerometer. (b) Z-axis sensing in the triaxis accelerometer. (c) X-axis sensing in the triaxis accelerometer.

equation for the lowest resonant frequency of the triaxis accelerometer:

$$f = \frac{1}{2\pi} \cdot \sqrt{\frac{48 \cdot \sum_i E_i \left(I_i + A_i Z_i^2\right)}{\rho \cdot L_\mathrm{m} \cdot W_\mathrm{m} \cdot H_\mathrm{m} \cdot l^3}} \tag{14}$$

where ρ, L_m, W_m, and H_m are the density, length, width, and thickness of the proof mass, respectively.

D. Effect of the In-Plane Residual Stress

The previous analysis ignores in-plane stress in the suspending beam, and this section analyzes the effect of in-plane residual stress on the sensitivity of the single- and triaxis accelerometers.

1) Single-Axis Piezoelectric-Bimorph Accelerometer Under In-Plane Residual Stress: Assuming that the residual stress results in a tensile axial force P, we analyze the effect of the axial force P on the sensitivity of the single-axis accelerometer, using Fig. 9(a) that shows a free-body diagram of the single-axis piezoelectric accelerometer, including the in-plane residual stress.

With pure torque M_0, Z-axis force F_0, and in-plane residual stress P applied to the suspending beam at the same time [Fig. 9(a)], we solve the governing differential equation, according to the boundary conditions, to obtain the bending moment in the beam as follows:

$$M(x) = -\frac{M_0 - \frac{F_0}{k} \cdot e^{-k\cdot l}}{e^{k\cdot l} + e^{-k\cdot l}} \cdot e^{k\cdot x} - \frac{M_0 + \frac{F_0}{k} \cdot e^{k\cdot l}}{e^{k\cdot l} + e^{-k\cdot l}} \cdot e^{-k\cdot x} \tag{15}$$

where $k = \sqrt{P/EI}$. Using (15) in (4) and integrating over the sensing electrode from $x = 0$ to $x = l$, the charge sensitivity on one sensing electrode of the single-axis accelerometer is

$$S_q = \frac{d_{31} \cdot E_\mathrm{p} \cdot z_\mathrm{p} \cdot m}{\sum_i E_i \left(\frac{1}{12} \cdot h_i^3 + h_i \cdot Z_i^2\right)} \cdot \left[\frac{1}{k^2} \cdot \left(\frac{1}{\cosh(k \cdot l)} - 1\right) - \frac{\frac{1}{2} \cdot L_\mathrm{m}}{k} \cdot \tanh(k \cdot l)\right]. \tag{16}$$

The calculated result shows that in-plane axial force has little effect on the charge sensitivity in the case of the single-axis accelerometer because of the cantilever-like structure.

2) Z-Axis Sensitivity in the Triaxis Piezoelectric-Bimorph Accelerometer Under In-Plane Residual Stress: Using Fig. 9(b) (that shows a free-body diagram of the triaxis piezoelectric accelerometer, including an axial force P due to in-plane residual stress), we obtain the following equation for the bending moment in the triaxis accelerometer that is built on bridge-like beams:

$$M(x) = \frac{\frac{F_0}{k} \cdot \left(1 - e^{-k\cdot l}\right)}{e^{k\cdot l} - e^{-k\cdot l}} \cdot e^{k\cdot x} + \frac{\frac{F_0}{k} \cdot \left(1 - e^{k\cdot l}\right)}{e^{k\cdot l} - e^{-k\cdot l}} \cdot e^{-k\cdot x} \tag{17}$$

where $k = \sqrt{P/EI}$.

Using (17) in (4) and integrating over the Z-axis sensing electrode in the triaxis accelerometer from $x = l/2$ to $x = l$ (Fig. 7), we obtain the Z-axis charge sensitivity on one sensing electrode of the triaxis piezoelectric accelerometer as follows:

$$S_q = \frac{d_{31} \cdot E_\mathrm{p} \cdot z_\mathrm{p} \cdot m}{\sum_i E_i \left(\frac{1}{12} \cdot h_i^3 + h_i \cdot Z_i^2\right)} \cdot \frac{1}{4 \cdot k^2} \cdot \left[1 - 2 \cdot \frac{\sinh\left(\frac{k\cdot l}{2}\right)}{\sinh(k \cdot l)}\right]. \tag{18}$$

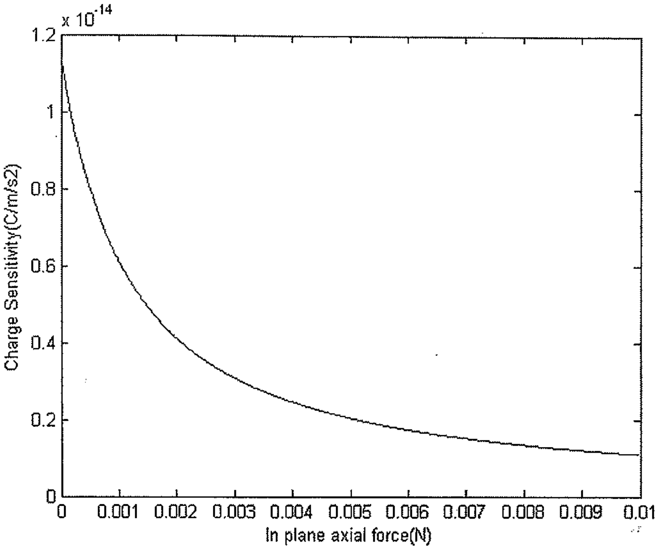

Fig. 10. Z-axis charge sensitivity of the triaxis piezoelectric-bimorph accelerometer as a function of an in-plane axial force (due to residual stress) in the suspending beams.

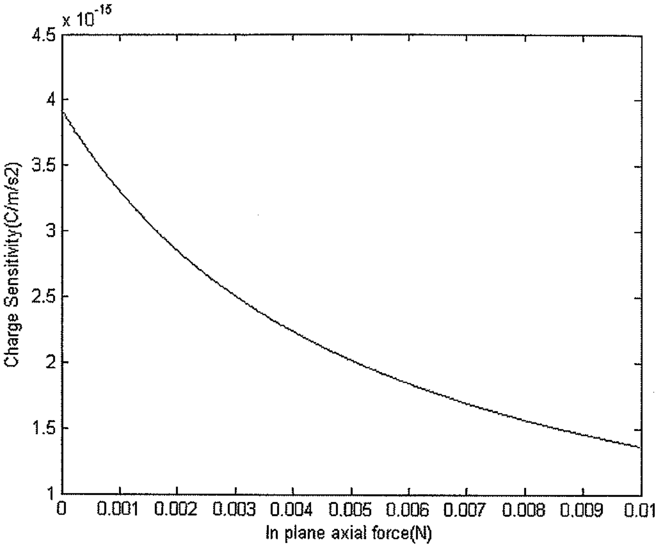

Fig. 11. X-axis charge sensitivity of the triaxis piezoelectric-bimorph accelerometer as a function of an in-plane axial force (due to residual stress) in the suspending beams.

TABLE III
DESIGNED STRUCTURE PARAMETERS AND EXPECTED CHARACTERISTICS FOR A TRIAXIS PIEZOELECTRIC-BIMORPH ACCELEROMETER

Beam length (μm)	340
Beam width (μm)	300
Al thickness (μm)	0.4
Al electrode length (μm)	130
Al electrode width (μm)	250
ZnO thickness (μm)	0.3
PECVD Si_xN_y thickness (μm)	0.1
Parylene thickness (μm)	2.1
Proof mass length (μm)	1700
Proof mass width (μm)	1700
Proof mass thickness (μm)	400
Expected Z-axis charge sensitivity (C/m/s^2)	1.14x10^{-14}
Expected X-axis charge sensitivity (C/m/s^2)	3.93x10^{-15}

Fig. 10 shows the calculation result of the Z-axis charge sensitivity (for a typical case of the triaxis piezoelectric-bimorph accelerometer with its structure parameters shown in Table III and the thickness of the parylene beam being equal to 2.1 μm) as a function of in-plane axial force (due to residual stress) in the multilayer beam of the triaxis accelerometer. The charge sensitivity decreases from 1.14×10^{-14} to 1.09×10^{-15} C/m/s^2 (more than ten times) by mere 0.01-N in-plane axial force, and we see that the triaxis accelerometer is heavily influenced by residual stress, as expected, since the suspending beams are like bridges with their two edges clamped.

3) X-/Y-Axis Sensitivity in the Triaxis Piezoelectric-Bimorph Accelerometer Under In-Plane Residual Stress: Using Fig. 9(c) (that shows the side view of the free-body diagram of the triaxis accelerometer when X-axis acceleration and in-plane residual tension stress are present at the same time), we solve the governing differential equation for the deflection of the suspending beam, according to the boundary conditions, to obtain the bending moment M in the suspending beam at location x

$$M(x) = \frac{\frac{3}{2} \cdot (l + L_{\mathrm{m}})}{k \cdot l^2} \cdot \frac{m \cdot \mathrm{acc} \cdot \frac{H_{\mathrm{m}}}{2}}{\left[\frac{2}{1+v} + 3 \cdot \left(1 + \frac{L_{\mathrm{m}}}{l}\right)^2\right] + \frac{P \cdot L_{\mathrm{m}} \cdot l}{2 \cdot \sum_i E_i \cdot \left(I_i + A_i \cdot Z_i^2\right)}} \cdot \left[\left(1 - \frac{1}{2} \cdot k \cdot l\right) \cdot e^{k \cdot x} - \left(1 + \frac{1}{2} \cdot k \cdot l\right) \cdot e^{-k \cdot x}\right] \tag{19}$$

where $k = \sqrt{(F_1 + P)/\sum_i E_i \cdot (I_i + A_i \cdot Z_i^2)} = \sqrt{[(1/2) \cdot m \cdot \mathrm{acc} + P]/\sum_i E_i \cdot (I_i + A_i \cdot Z_i^2)}$, whereas F_1 is the lateral force applied on the suspension beam by the fixed boundary, and P is the axial force due to in-plane residual stress.

Using (19) in (4) and integrating along the length of the X-axis sensing electrode (Fig. 7), we obtain the X-axis charge sensitivity of the triaxis accelerometer under in-plane tension force P as follows:

$$S_q = \frac{d_{31} \cdot E_{\mathrm{p}} \cdot z_{\mathrm{p}}}{\sum_i E_i \left(\frac{1}{12} \cdot h_i^3 + h_i \cdot Z_i^2\right)} \cdot \frac{(l + 3 \cdot L_{\mathrm{m}})}{8} \cdot \frac{m \cdot \frac{H_{\mathrm{m}}}{2}}{\left[\frac{2}{1+v} + 3 \cdot \left(1 + \frac{L_{\mathrm{m}}}{l}\right)^2\right] + \frac{P \cdot L_{\mathrm{m}} \cdot l}{2 \cdot \sum_i E_i \cdot \left(I_i + A_i \cdot Z_i^2\right)}}. \tag{20}$$

From (20), we can see that the X-axis charge sensitivity in the triaxis accelerometer decreases when the residual stress force P increases. Fig. 11 shows the calculation result of the X-axis charge sensitivity (for a typical case of the triaxis piezoelectric-bimorph accelerometer with its structure parameters shown in Table III and the thickness of the parylene beam being equal to 2.1 μm) as a function of in-plane axial force (due to residual stress) in the multilayer beam of the

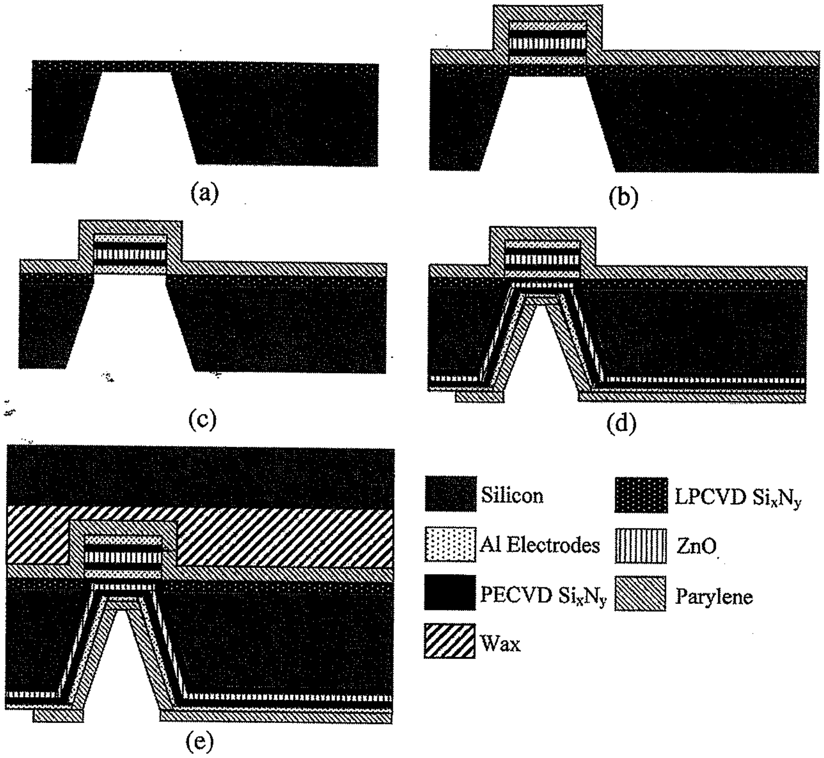

Fig. 12. Fabrication process of the single-axis piezoelectric-bimorph accelerometer. (a) Bulk-micromachined Si. (b) Deposit and pattern 0.4-μm Al, 0.1-μm PECVD $\mathrm{Si}_x\mathrm{N}_y$, 0.3-$\mu$m ZnO, 0.1-$\mu$m PECVD $\mathrm{Si}_x\mathrm{N}_y$, 0.4-$\mu$m Al, and 3.7-$\mu$m parylene on the wafer front side. (c) Etch $\mathrm{Si_3N_4}$ from the wafer backside. (d) Deposit 0.1-μm PECVD $\mathrm{Si}_x\mathrm{N}_y$, 0.3-$\mu$m ZnO, 0.1-$\mu$m PECVD $\mathrm{Si}_x\mathrm{N}_y$, 0.4-$\mu$m Al, and 3.7-$\mu$m parylene on the wafer backside. (e) We use wax to fix the wafer to a dummy wafer and dice the wafer to form a beam-mass structure.

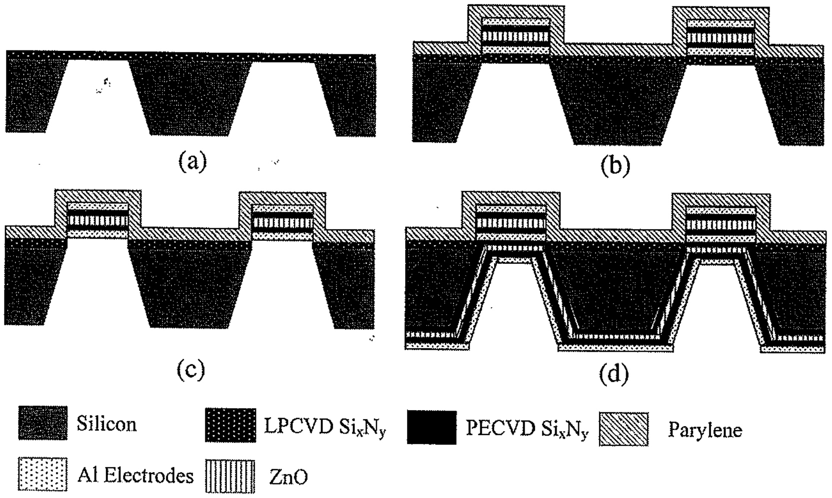

Fig. 13. Fabrication process of the triaxis piezoelectric-bimorph accelerometer. (a) Bulk-micromachined Si. (b) Deposit and pattern 0.4-μm Al, 0.1-μm PECVD $\mathrm{Si}_x\mathrm{N}_y$, 0.3-$\mu$m ZnO, 0.1-$\mu$m PECVD $\mathrm{Si}_x\mathrm{N}_y$, 0.4-$\mu$m Al, and 2.1-$\mu$m parylene on the wafer front side. (c) Etch $\mathrm{Si_3N_4}$ from the wafer backside. (d) Deposit 0.1-μm PECVD $\mathrm{Si}_x\mathrm{N}_y$, 0.3-$\mu$m ZnO, 0.1-$\mu$m PECVD $\mathrm{Si}_x\mathrm{N}_y$, and 0.4-$\mu$m Al on the wafer backside.

triaxis accelerometer. The charge sensitivity decreases from 3.93×10^{-15} to 1.36×10^{-15} C/m/s^2 (by 2.9 times) due to 0.01-N in-plane axial force.

IV. FABRICATION

The main fabrication steps for the single- and triaxis piezoelectric-bimorph accelerometers are similar to each other. The fabrication processes for the single- and triaxis accelerometers are briefly shown in Figs. 12 and 13, respectively, and are described in the succeeding sections.

A. Single-Axis Piezoelectric-Bimorph Accelerometer

Following the steps shown in Fig. 12, we first form a 0.8-μm-thick $\mathrm{Si}_x\mathrm{N}_y$ diaphragm on a silicon wafer by KOH etching, which is followed by deposition and patterning of 0.4-μm-thick Al, 0.1-μm-thick PECVD $\mathrm{Si}_x\mathrm{N}_y$, 0.3-$\mu$m-thick ZnO, 0.1-$\mu$m-thick PECVD $\mathrm{Si}_x\mathrm{N}_y$, 0.4-$\mu$m-thick Al, and 3.7-$\mu$m-thick parylene film on the front side of the wafer. The ZnO is electrically insulated through two 0.1-μm-thick PECVD $\mathrm{Si}_x\mathrm{N}_y$ films for static response of the accelerometer. After etching away the $\mathrm{Si_3N_4}$ diaphragm from the wafer backside,

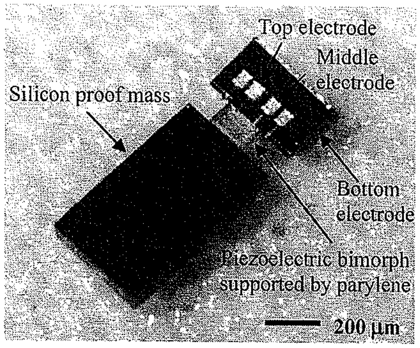

Fig. 14. Front-side photo of a completed single-axis piezoelectric-bimorph accelerometer.

we deposit 0.1-μm-thick PECVD Si_xN_y insulating layer, 0.3-μm-thick ZnO, 0.1-μm-thick PECVD Si_xN_y, 0.4-μm-thick Al, and 3.7-μm-thick parylene supporting layer on the wafer backside for the bottom half of the bimorph. The bimorph beams are formed by etching away most of the diaphragm through reactive-ion etching (RIE). Finally, the silicon wafer is glued to a dummy wafer with wax and is diced to form the beam-mass structure with vertical sidewalls.

B. Triaxis Piezoelectric-Bimorph Accelerometer

Following the fabrication steps shown in Fig. 13, we first form a 0.8-μm-thick Si_xN_y diaphragm, producing a proof-mass silicon island (by KOH etching with a proper convex corner compensation) in the middle of the Si_xN_y diaphragm. Then, 0.4-μm-thick Al, 0.1-μm-thick PECVD Si_xN_y, 0.3-μm-thick ZnO, 0.1-μm-thick PECVD Si_xN_y, 0.4-μm-thick Al, and 2.1-μm-thick parylene film are deposited and patterned on the front side of the wafer. After etching away the Si_3N_4 diaphragm from the wafer backside, we deposit 0.1-μm-thick PECVD Si_xN_y insulating layer, 0.3-μm-thick ZnO, 0.1-μm-thick PECVD Si_xN_y, and 0.4-μm-thick Al on the wafer backside for the bottom half of the bimorph. Then, we form the bimorph beams by etching away a portion of the diaphragm through RIE, which is followed by dicing of the wafer into individual chips.

Fig. 14 shows the front-side view of a fabricated single-axis piezoelectric-bimorph accelerometer, whereas Fig. 15 shows the front-side and backside views of a completed triaxis piezoelectric-bimorph accelerometer.

V. EXPERIMENTAL SETUP

Fig. 16 shows a schematic of the experimental setup for measuring the sensitivity and resonant frequency of a piezoelectric accelerometer. A fabricated accelerometer chip and a voltage amplifier on a printed circuit board are housed in a metal box to shield out electromagnetic interference. A vibration exciter is used to provide acceleration force to the accelerometer chip. A commercial accelerometer ADXL202 from Analog Devices, Inc. is used to calibrate the vibration system. We use a voltage amplifier rather than a charge amplifier since a voltage amplifier gives a higher signal-to-noise ratio in case of relatively small charge developed. The piezoelectric-bimorph accelerometer and its amplifying circuitry are modeled by the equivalent circuit shown in Fig. 17. A diode D is used to provide a very high resistance so that a tiny leakage path will be present to drain off stray charges that might accumulate on the exposed electrode. The voltage at the input of the voltage amplifier is

$$V_{\mathrm{m}} = \frac{Q}{C_{\mathrm{p}} + C_{\mathrm{e}} + C_{\mathrm{p}} \cdot C_{\mathrm{e}} \cdot \frac{1}{C_0}} \tag{21}$$

where Q is the total charge produced on the sensing electrode, C_{p} is the composite capacitance across the ZnO layer and the electrically insulating PECVD Si_xN_y layer covering the ZnO [22], and C_{e} is the parasitic capacitance (measured to be 11.56 pF) due to the amplifier, the diode, and the conductor line connecting the accelerometer to the amplifier. Fig. 18 shows the typical outputs of the bimorph piezoelectric accelerometer and ADXL202 when sinusoidal signal is applied to the vibration exciter.

VI. EXPERIMENTAL RESULTS AND DISCUSSION

A. Single-Axis Piezoelectric-Bimorph Accelerometer

A few different designs of the single-axis piezoelectric-bimorph accelerometer with different suspension-beam widths and electrode areas have been fabricated and tested. The structure parameters of one such design and its expected characteristics are listed in Table IV. The frequency response of the fabricated piezoelectric accelerometer for a 1-g constant acceleration (Fig. 19) is measured to have a flat response from subhertz to 60 Hz, with a resonant frequency around 98 Hz. Fig. 20 shows the low-frequency response of the fabricated accelerometer. The achievable low-frequency response (down to quasi-dc) depends on the effective impedance of the detection circuit in Fig. 17. With the current detection circuitry, the achievable minimum detectable frequency is 0.1 Hz. The measured unamplified sensitivity of the bimorph piezoelectric accelerometer is around 7.0 mV/g in the flat frequency range, and the minimum detectable signal level is around 0.01 g, with most of the noise coming from the detecting-circuit noise. The accelerometer output is measured as a function of acceleration amplitude and is shown to have a linearity of 0.9% up to 3 g (Fig. 21).

Table V summarizes the calculation and measurement results for the single-axis piezoelectric-bimorph accelerometer, with the structure parameters listed in Table IV. The measured resonant frequency is a little lower than the calculated value, possibly due to the actual Young's moduli of the multilayer suspending beam being smaller than the ones used in the calculation. The measured voltage sensitivity (7.0 mV/g) is a little lower than the calculated value (8.3 mV/g), partly due to d_{31} of the ZnO film being less in the real device than the one used in the calculation. The residual stress in the suspending beam is expected to affect the sensitivity only slightly since the beam is essentially a cantilever.

B. Triaxis Piezoelectric-Bimorph Accelerometer

Fig. 22 shows the triaxis accelerometer outputs on the X-, Y-, and Z-axis electrodes as a function of acceleration amplitude

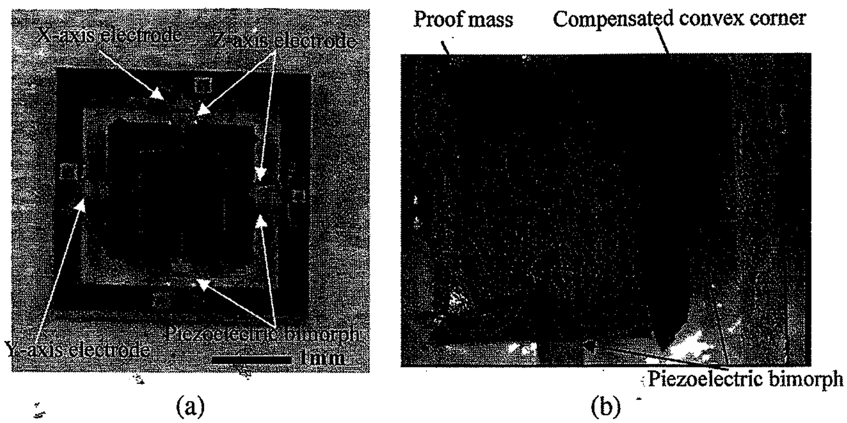

(a) (b)

Fig. 15. Photos of a completed triaxis piezoelectric-bimorph accelerometer. (a) Front side. (b) Backside.

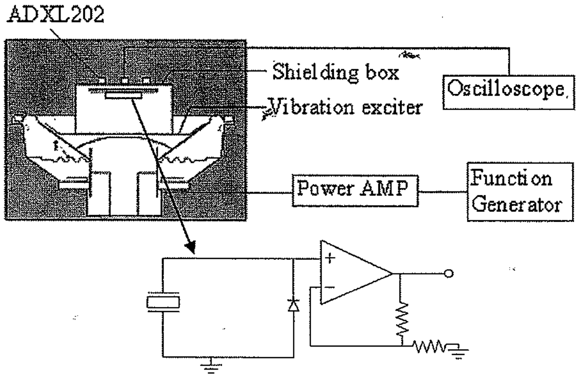

Fig. 16. Testing setup for the piezoelectric accelerometers.

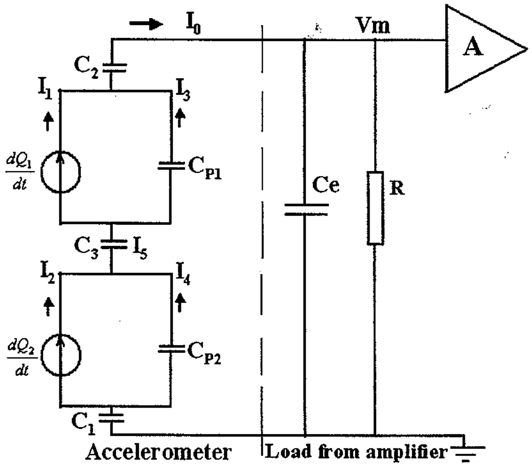

Fig. 17. Equivalent circuit of the single-axis piezoelectric-bimorph accelerometer along with the loading from the detection circuit.

when the acceleration is applied along X-, Y-, and Z-axes, respectively. The unamplified sensitivities of the X-, Y-, and Z-axis electrodes in response to accelerations in X-, Y-, and Z-axes are measured to be 0.93, 1.13, and 0.88 mV/g, respectively.

Figs. 23 and 24 show the accelerometer outputs on the X-, Y-, and Z-axis electrodes when the acceleration is applied only along the X- or Y-axis. The figures show that the cross-axial sensitivity among the X-, Y-, and Z-axis electrodes is less than 15%. The measurement results of the cross-axial sensitivity include not only the output from the accelerometer chip itself but also the noise picked up by the circuit. The noise spectrum of the output signal is measured with a spectrum analyzer, and the minimum detectable signal is estimated to be 0.04 g over a 100-Hz bandwidth (Fig. 25).

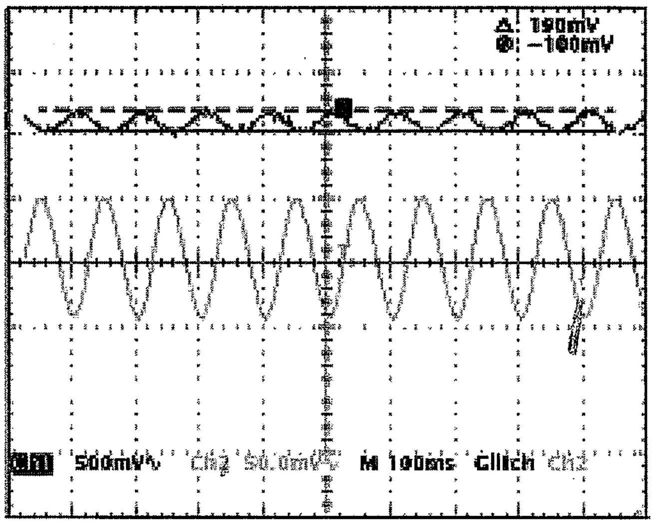

Fig. 18. Typical measured outputs of the single-axis piezoelectric-bimorph accelerometer (bottom curve) and of the commercial ADXL202 (top curve) when a sinusoidal acceleration of same amplitude is applied to both accelerometers.

TABLE IV
STRUCTURE PARAMETERS IN THE COMPLETED DEVICE AND EXPECTED CHARACTERISTICS FOR THE SINGLE-AXIS PIEZOELECTRIC-BIMORPH ACCELEROMETER

Beam length (μm)	140
Beam width (μm)	1000
Al thickness (μm)	0.4
Al electrode length (μm)	40
Al electrode width (μm)	1000
ZnO thickness (μm)	0.3
PECVD Si_xN_y thickness (μm)	0.1
Parylene thickness (μm)	3.7
Proof mass length (μm)	2150
Proof mass width (μm)	1200
Proof mass thickness (μm)	330
Expected resonant frequency (Hz)	131
Expected charge sensitivity(C/m/s^2)	2.36×10^{-14}

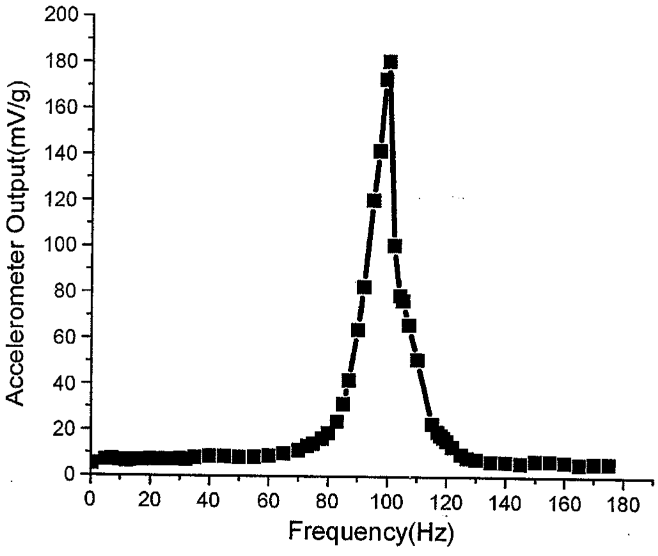

Fig. 19. Measured frequency response of the single-axis piezoelectric-bimorph accelerometer.

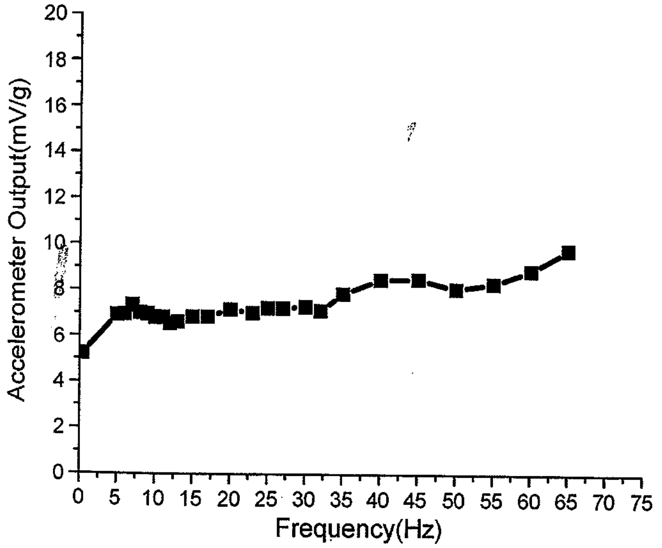

Fig. 20. Measured low-frequency response of the single-axis accelerometer showing an unamplified sensitivity of about 7 mV/g.

Table VI summarizes the simulated and measured results for the triaxis piezoelectric-bimorph accelerometer, with its structure parameters listed in Table III. The measured Z-axis voltage sensitivity is about 12 times lower than the sensitivity calculated without considering the residual stress effect (though the measured X-axis voltage sensitivity is close to the calculated value), demonstrating the significant effect of the residual stress on the Z-axis sensitivity of the triaxis piezoelectric-bimorph accelerometer. The residual stress affects the Z-axis sensitivity much more significantly than the X-/Y-axis sensitivity, as can be seen from the prior theoretical analysis.

VII. SUMMARY

Novel single- and triaxis piezoelectric-bimorph accelerometers have been designed, fabricated, and tested for low-frequency applications such as human-body-movement sensing. A piezoelectric-bimorph structure of parylene/Al/Si_xN_y/ZnO/Si_xN_y/Al/Si_xN_y/ZnO/Si_xN_y/Al/parylene is fabricated by depositing a ZnO film on both sides of the wafer and is mechanically supported mainly by parylene. With the neutral plane fixed just at the middle of the beam thickness and the two piezoelectric layers above and below the neutral plane, the sensitivity is maximized. The sensitivity is improved also because of the low stiffness of a parylene layer supporting

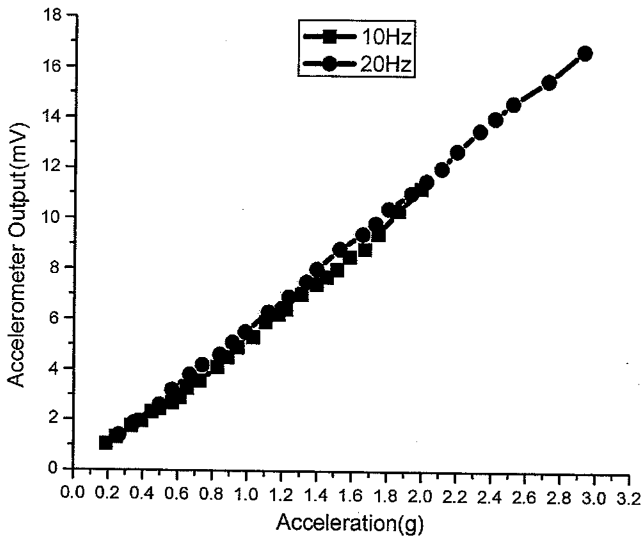

Fig. 21. Measured unamplified output of the single-axis accelerometer versus acceleration amplitude.

TABLE V
CALCULATED AND MEASURED CHARACTERISTICS OF THE SINGLE-AXIS PIEZOELECTRIC-BIMORPH ACCELEROMETER

		Calculated	Measured
Sensitivity	Charge sensitivity on one electrode (fC/g)	231	
	Voltage sensitivity (mV/g)	8.3	7.0
Resonant frequency(Hz)		131	98

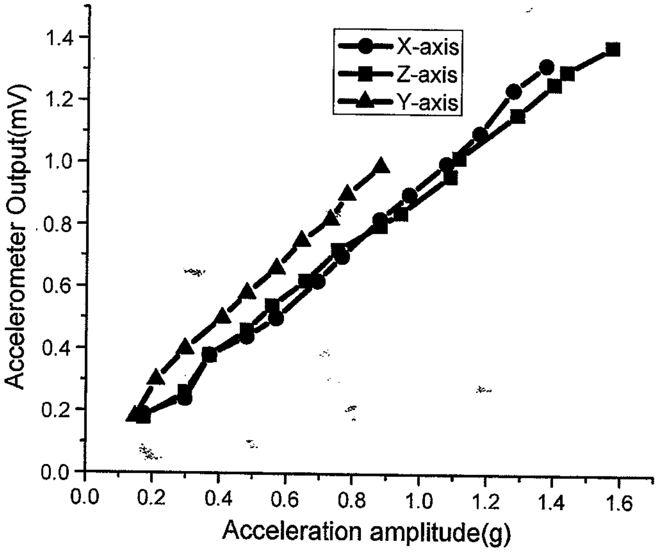

Fig. 22. Measured unamplified outputs on the X-, Y-, and Z-axis electrodes of the triaxis accelerometer (for 20-Hz accelerations applied along X-, Y-, and Z-axes, respectively) as a function of acceleration amplitude.

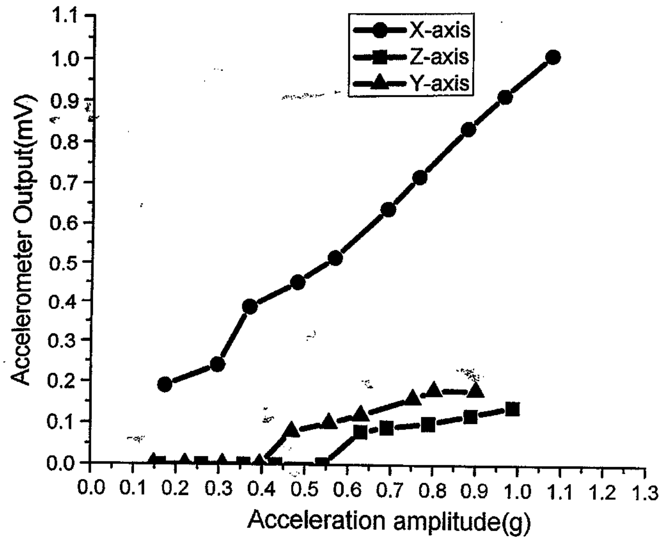

Fig. 23. Measured unamplified outputs on the X-, Y-, and Z-axis electrodes (of the triaxis accelerometer) for 20-Hz accelerations applied along X-axis as a function of acceleration amplitude.

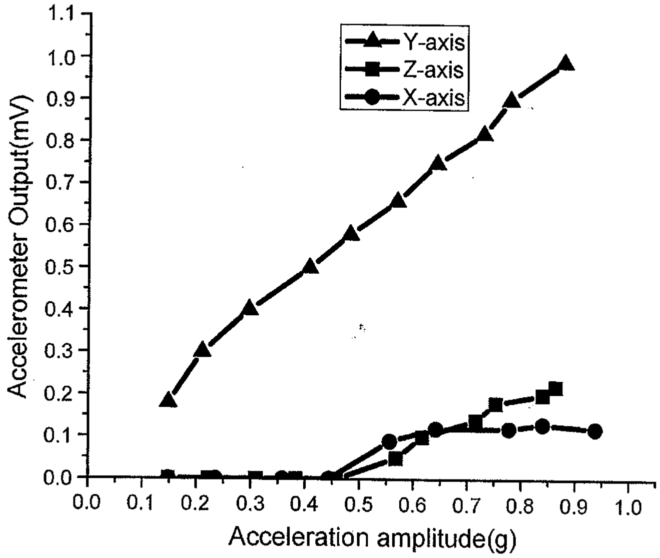

Fig. 24. Measured unamplified outputs on the X-, Y-, and Z-axis electrodes (of the triaxis accelerometer) for 20-Hz accelerations applied along Y-axis as a function of acceleration amplitude.

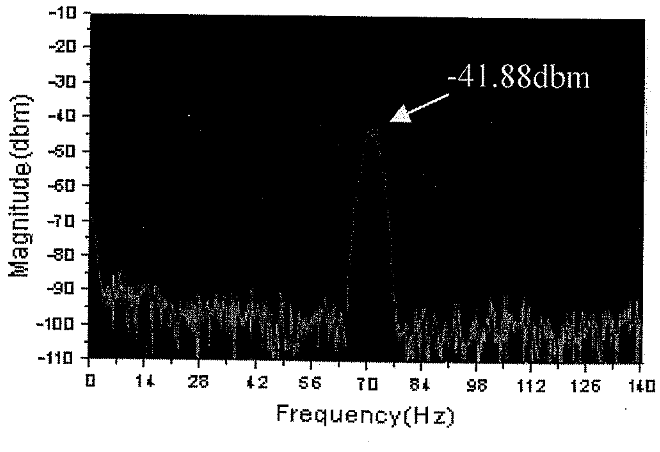

Fig. 25. Output (Z-axis) of the triaxis accelerometer measured by a spectrum analyzer for a 70-Hz 1-g acceleration applied in Z-axis.

TABLE VI
SIMULATED AND MEASURED CHARACTERISTICS OF THE TRIAXIS PIEZOELECTRIC-BIMORPH ACCELEROMETER

		Calculated	Measured
X-axis sensitivity	Charge sensitivity on one electrode(fC/g)	38.5	
	Voltage sensitivity(mV/g)	1.59	0.93
Y-axis sensitivity	Charge sensitivity on one electrode(fC/g)	38.5	
	Voltage sensitivity(mV/g)	1.59	1.13
Z-axis sensitivity	Charge sensitivity on one electrode(fC/g)	111.7	
	Voltage sensitivity(mV/g)	10.89	0.88

the beam. Quasi dc response is achieved by incorporating electrically insulating layer on both sides of the ZnO film. The fabricated single-axis piezoelectric-bimorph accelerometer is measured to have an unamplified sensitivity of 7 mV/g and 0.01-g resolution. The fabricated triaxis accelerometer has unamplified sensitivities of 0.9, 1.13, and 0.88 mV/g on X-, Y-, and Z-axes, respectively. The cross-axis sensitivity is minimized due to the highly symmetric quad-beam structure.

ACKNOWLEDGMENT

This material is based upon the work supported by NIH Grant R01 HD39099.

REFERENCES

[1] T. Berther, G. H. Gautschi, and J. Kubler, "Capacitive accelerometers for static and low-frequency measurements," *Sound Vib.*, vol. 30, no. 6, pp. 28–30, 1996.

[2] H. Chen, S. Shen, and M. Bao, "Over-range capacity of a piezoresistive microaccelerometer," *Sens. Actuators A, Phys.*, vol. 58, no. 3, pp. 197–201, Mar. 1997.

[3] D. W. Stachell and J. C. Greenwood, "A thermally-excited silicon accelerometer," *Sens. Actuators*, vol. 17, no. 1/2, pp. 241–245, May 1989.

[4] R. L. Kubena, G. M. Atkinsin, W. P. Robinson, and F. P. Stratton, "A new miniaturized surface micromachined tunneling accelerometer," *IEEE Electron Device Lett.*, vol. 17, no. 6, pp. 306–308, Jun. 1996.

[5] U. A. Dauderstadt, P. H. S. de Vries, R. Hiratsuka, and P. M. Sarro, "Silicon accelerometer based on thermopiles," *Sens. Actuators A, Phys.*, vol. 46/47, no. 1–3, pp. 201–204, Jan./Feb. 1995.

[6] P. L. Chen, R. S. Muller, R. D. Jolly, G. L. Hallac, R. M. White, A. P. Andrews, T. C. Lim, and M. E. Motamedi, "Integrated silicon microbeam PI-FET accelerometer," *IEEE Trans. Electron Devices*, vol. ED-29, no. 1, pp. 27–33, Jan. 1982.

[7] G. E. Loeb, R. A. Peck, W. H. Moore, and K. Hood, "BION system for distributed neural prosthetic interface," *J. Med. Eng. Phys.*, vol. 23, pp. 9–11, 2001.

[8] M. E. Motamedi, A. P. Andrews, and E. Brower, "Accelerometer sensor using piezoelectric ZnO thin films," in *Proc. IEEE Ultrason. Symp.*, 1982, vol. 1, pp. 303–307.

[9] K. Okada, "Tri-axial piezoelectric accelerometer," in *Proc. Transducers*, 1995, pp. 566–569.

[10] P. Scheeper, J. O. Gullov, and L. M. Kofoed, "A piezoelectric triaxial accelerometer," *J. Micromech. Microeng.*, vol. 6, no. 1, pp. 131–133, Mar. 1996.

[11] J. Yu and C. Lan, "System modeling of microaccelerometer using piezoelectric thin films," *Sens. Actuators A, Phys.*, vol. 88, no. 2, pp. 178–186, Feb. 2001.

[12] D. L. DeVoe and A. P. Pisano, "A fully surface-micromachined piezoelectric accelerometer," in *Proc. Transducers*, 1997, pp. 1205–1208.

[13] D. L. DeVoe and A. P. Pisano, "Surface micromachined piezoelectric accelerometers," *J. Microelectromech. Syst.*, vol. 10, no. 2, pp. 180–185, Jun. 2001.

[14] R. de Reus, J. O. Gullov, and P. R. Scheeper, "Fabrication and characterization of a piezoelectric accelerometer," *J. Micromech. Microeng.*, vol. 9, no. 2, pp. 123–126, 1999.

[15] G. Li, Z. Li, Y. Jin, Y. Hao, D. Zhang, and G. Wu, "Design and simulation of capacitive, piezoresistive and piezoelectric triaxial accelerometers using a highly symmetrical quad-beam structure," in *Proc. 11th Int. Conf. Solid State Sens. Actuators*, Munich, Germany, Jun. 10–14, 2001, pp. 304–307.

[16] M. Niu and E. S. Kim, "Bimorph piezoelectric acoustic transducer," in *Proc. 11th Int. Conf. Solid State Sens. Actuators*, Munich, Germany, Jun. 10–14, 2001, pp. 110–113.

[17] C. H. Han and E. S. Kim, "Parylene-diaphragm piezoelectric acoustic transducers," in *Proc. IEEE Int. Mico Electo Mechan. Syst. Conf.*, Miyazaki, Japan, 2000, pp. 148–152.

[18] M. Niu and E. S. Kim, "Piezoelectric bimorph microphone built on micromachined parylene diaphragm," *J. Microelectromech. Syst.*, vol. 12, no. 6, pp. 892–898, Dec. 2003.

[19] P. L. Chen, R. S. Muller, R. M. White, and R. Jolly, "Thin film ZnO-MOS transducer with virtually DC response," in *Proc. IEEE Ultrasonics Symp.*, Boston, MA, Nov. 5–7, 1980, pp. 945–948.

[20] M. S. Weinberg, "Working equations for piezoelectric actuators and sensors," *J. Microelectromech. Syst.*, vol. 8, no. 4, pp. 529–533, Dec. 1999.

[21] A. Kovacs and Z. Vizvary, "Structure parameters sensitivity analysis of cantilever- and bridge-type accelerometers," *Sens. Actuators A, Phys.*, vol. 89, no. 3, pp. 197–205, 2001.

[22] E. S. Kim, "Integrated microphone with CMOS circuit on a single chip," Ph.D. dissertation, Univ. California, Berkeley, Berkeley, CA, 1990.

Qiang Zou (S'05–M'05) received the B.S. degree in material science and M.S. degree in electrical engineering from Shanghai Jiao Tong University, Shanghai, China, in 1992 and 1995, respectively, and the Ph.D. degree in electrical engineering from the University of Southern California (USC), Los Angeles, in 2005. His doctoral dissertation was on the microelectromechanical systems (MEMS) inertial sensors for biomedical and automotive application.

In 1995, he joined the State Key Laboratory of Transducer Technology, Shanghai Institute of Microsystem and Information Technology, Chinese Academy of Sciences, Shanghai, as a MEMS Researcher, working on the micromachining capacitive accelerometer and other MEMS devices. In 1998, he joined the Institute of Materials Research and Engineering, National University of Singapore, Singapore, as a MEMS Research Officer, working on optical and RF MEMS. From 1999 to 2001, he was a Ph.D. Graduate Research Assistant with the Department of Electrical Engineering, University of Hawaii at Manoa, Honolulu. Subsequently, he was with Intel Corporation as an Engineering Intern in Summer 2001. From 2001 to 2005, he was a Graduate Research Assistant with the Department of Electrical Engineering, USC, where continued his Ph.D. studies. After graduating from USC in 2005, he joined the Siimpel Corporation, Arcadia, CA, and was the Manager of the New Products and Processes Group. He is currently with the Wireless Semiconductor Division, Avago Technologies, Ltd., San Jose, CA. His research interests include MEMS, MEMS inertial sensors, acoustic and piezoelectric transducers, optical MEMS, mechanical modeling and FEA simulation, and microfabrication processing technology.

Wei Tan, photograph and biography not available at the time of publication.

Eun Sok Kim (M'91–SM'01) received the B.S. (high honors), M.S., and Ph.D. degrees in electrical engineering from the University of California, Berkeley, in 1982, 1987, and 1990, respectively. His doctoral dissertation was on the integrated microphone with LSI CMOS on a single chip.

He was with the IBM Research Laboratory, San Jose, CA, NCR Corporation, San Diego, CA, and Xicor Inc., Milpitas, CA, as a Co-op Student, Design Engineer, and Summer-Student Engineer, respectively. From Spring 1991 to Fall 1999, he was with the Department of Electrical Engineering, University of Hawaii (UH) at Manoa, Honolulu, as a Faculty Member. Since Fall 1999, he has been with the University of Southern California, Los Angeles, where he is currently a Professor with the Department of Electrical Engineering. His research interests include microelectromechanical systems, acoustic and piezoelectric transducers, microfluidic systems, microfabrication processing technology, and materials study. He serves on the editorial board of the *Journal of Micromechanics and Microengineering*.

Dr. Kim is a recipient of a Research Initiation Award (1991–1993) and a Faculty Early Career Development Award (1995–1999) from the National Science Foundation. He received the Outstanding Electrical Engineering Faculty of the Year Award (voted by UH IEEE Student Chapter) in May 1996.

Gerald E. Loeb (M'98) received the B.A. and M.D. degrees from The Johns Hopkins University, Baltimore, MD, in 1969 and 1972, respectively.

After graduating, he did one year of surgical residency at the University of Arizona, Tucson. From 1973 to 1988, he was with the Laboratory of Neural Control, National Institutes of Health, Bethesda, MD. From 1988 to 1999, he was a Professor of physiology and biomedical engineering with Queen's University, Kingston, ON, Canada. From 1994 to 1999, he was with the Advanced Bionics Corporation, the manufacturer of the Clarion cochlear implant, as the Chief Scientist and one of the original developers of the cochlear implant to restore hearing to the deaf. He is currently a Professor of biomedical engineering and the Director of the Medical Device Development Facility of the Alfred E. Mann Institute for Biomedical Engineering, University of Southern California, Los Angeles. He is the holder of 38 issued U.S. patents. He is the author of more than 200 scientific papers. Most of his current research is directed toward neural prosthetics to reanimate paralyzed muscles and limbs using a new technology that he and his collaborators developed called BIONs. This work is supported by an NIH Bioengineering Research Partnership and is one of the testbeds in the NSF Engineering Research Center on Biomimetic MicroElectronic Systems, for which he is the Deputy Director. These clinical applications build on his longstanding basic research into the properties and natural activities of muscles, motoneurons, proprioceptors, and spinal reflexes.

Dr. Loeb is a Fellow of the American Institute of Medical and Biological Engineers.